Characterisation of Carbonaceous Deposits on Diesel Injector Nozzles

Catriona M. McGilvery[1*], Jun Jiang[1,2], Nicholas J. Rounthwaite[3], Rod Williams[4], Finn Giuliani[1] and T. Ben Britton[1]

1. Department of Materials, Imperial College London, SW7 2AZ
2. Department of Mechanical Engineering, Imperial College London, SW7 2AZ
3. Shell Global Solutions, Shell Centre, London, SE1 7NA
4. Shell Global Solutions, 40 Bank Street, London, E14 5NR

* Corresponding author: catriona.mcgilvery@imperial.ac.uk

Keywords: electron microscopy, organic depositions, fuel systems

Highlights:

1. Nanometre scale chemical characterisation of carbon rich depositions on the surface of diesel injector nozzles have been performed.
2. Depositions from vehicle chassis dynamometer and bench engine based dirty-up tests have been compared.
3. The structure and chemical compositions, and layer based growth of the depositions are explored, revealing elemental stratification.

Abstract

Diesel injector nozzles are highly engineered components designed to optimise delivery of fuel into the combustion chamber of modern engines. These components contain narrow channels to enhance spray formation and penetration, hence mixing and combustion. Over time, these injectors can become clogged due to fouling by carbonaceous deposits which may affect the long-term performance of a diesel engine. In this paper, we explore the chemical composition and structure of deposits formed within the nozzle, at the nanometre scale using electron microscopy. We focus on comparing deposits generated using a chassis dynamometer-based test with Zn fouled fuel with a DW10B dirty up test. We have developed and applied a method to precisely section the deposits for 'top view' scanning electron microscopy (SEM) and energy dispersive X-ray spectroscopy (EDS) analysis of the morphology and relative accumulation of deposits formed during chassis

dynamometer and engine based dirty-up tests. We extend this analysis to finer length scales through lift out of ~70 nm thick electron transparent cross section foils, including both the metal substrate and deposit, using focussed ion beam (FIB) machining. These foils are analysed using scanning transmission electron microscopy (STEM) and STEM-EDS. These thin foils reveal thin-film growth and chemical stratification of Zn, C, O and other elements in the organic deposit layers developed during growth on the steel substrate during industry standard fouling tests.

(1) Introduction

Modern diesel vehicles rely on high precision injector nozzles to ensure that fuel is delivered to the cylinder with precise spray formation, penetration and momentum. In turn, this facilitates efficient fuel-air mixing, hence efficient combustion. Deposits forming in the injector nozzle holes of modern diesel vehicles can reduce the fuel injected into the combustion chamber [1-4] and disrupt atomisation. This can lead to reduced or less efficient combustion, resulting in reduction in power and increased fuel consumption and emissions [5-7]; therefore there is a great deal of interest in studying these deposits with the ultimate aim of reducing their formation.

From prior studies in this field [8-9] it can be concluded that the propensity for formation of such deposits is influenced primarily by operating conditions (driving pattern and style), fuel quality and the inherent sensitivity of the vehicle hardware.

The Co-ordinating European Council's direct injection common rail diesel engine injector nozzle coking test, CEC F-098 (DW10B test) [10] is the industry standard test for evaluating fuel and additive effects on injector nozzle coking (fouling) in European diesel passenger cars with Direct Injection (DI) engines. The test uses a Peugeot DW10B Euro 4 build common rail engine and relies on fouling-sensitised injectors, with zinc as a fuel pro-foulant and a test cycle dominated by high load to achieve measurable fouling levels determined by power loss. This provides an opportunity to subsequently examine the structure and chemistry of the deposits forming in the nozzle during the test, and deposit examination can also be performed after similar chassis dynamometer (CD) testing.

Previous work to understand the formation and composition of injector nozzle deposits is limited, partly due to the inaccessibility of the deposits and difficulties of preserving them when the nozzle is dissected to access them. In an analysis of a cross-sectioned diesel injector from a medium-duty truck engine, Tang *et al.* showed that the deposit composition changed through the cross-section; in particular zinc appeared to be concentrated close to the metal surface of the nozzle and the deposit became more carbonaceous away from the metal interface as it grew thicker [11]. Variation in

chemical composition through the deposit indicates that the deposit may form an initiation layer followed by a thicker secondary layer on top, in a growth mechanism which might not be uniform across the length of the injector nozzle. A study by Ikemoto *et al.* examining deposits inside light-duty (LD) engine injectors [12] concluded that in the initial phase of deposit formation, low molecular weight ('lower') zinc carboxylate formed close to the nozzle hole outlet by reactions between zinc in the fuel and lower carboxylic acid in the combustion gas. In the subsequent growth phase, the main component changed to zinc carbonate close to the nozzle hole inlet by reactions with CO_2 in the combustion gas.

Analysis methods such as scanning electron microscopy (SEM) and energy dispersive X-ray spectroscopy (EDS) have been used in the aforementioned studies to investigate deposit composition and structure to provide insights on deposit formation mechanisms. Barker *et al* combined a number of techniques (fourier-transform infrared spectroscopy, profilometry, scanning electron microscopy, time of flight secondary ion mass spectroscopy, and direct analaysis in real time mass spectroscopy) to obtain morphological, chemical and compositional data from nozzles [13]. However, there remains a significant gap in knowledge when it comes to understanding the initial mechanism which causes fuel deposits to form on the nozzle surface. Although the effect that inhibits fuel flow is on the macro scale, the problem of deposition will never be fully understood or tackled until the deposition mechanisms which occur on the nanoscale are properly understood.

Understanding the sub-surface structure, and nanoscale interactions between the deposit and the steel surface of the nozzle are not easy tasks. SEM and EDS are only sensitive to the surface chemistry and morphology, and analysis of variable density 'foams' of light elements on a metallic substrate is difficult. Deposits vary in thickness up to tens of microns in depth and it is impossible to characterise the structure beneath the surface or the interface interactions using these methods. The only way to probe the underlying structure and investigate interfaces is to section them, and ultimately perform higher resolution transmission electron microscopy (TEM) of thin cross sections, which requires careful specimen preparation. Modern focussed ion beam systems are well established for TEM lift out, but in these engineering components the geometry and the fragile structure of the deposition layer adds significant challenges for thin foil preparation required to enable high quality TEM analysis.

In this manuscript, we demonstrate how samples can be prepared for TEM through careful sectioning of the nozzles and subsequent focussed ion beam SEM (FIB-SEM) cross section sample preparation from specific regions of interest in the nozzle. We apply this to two injector samples:

the first from a DW10B engine test following the CEC method, [10] and the other from a diesel vehicle having undergone testing on a chassis dynamometer (CD) following a Shell in-house method [14]. Both samples have previously been studied previously exploring power loss associated with injector fouling with deposit microstructure analysis, using SEM and EDS [15-16]. Both samples were prepared for TEM and the underlying structure and chemistry probed using scanning transmission electron microscopy (STEM) and EDS. The cross section allows the underlying structure to be studied with nanometre spatial resolution which, combined with EDS, allows chemical analysis on the nanoscale to be achieved.

(2) Instrumentation and Methods:

Samples

Two sets of injectors were used for this study (see Table 1):

Set one, so called 'CD DU', were taken from a diesel vehicle with mini-sac nozzles which underwent testing on a chassis dynamometer (CD) with CEC fuel containing 1mg/kg Zn known to produce fouling in engines [7,9,14]. This test is designed to simulate real-world fouling operating conditions and chemistry.

Set two, so called 'DW10B DU', were taken from an engine having run a 32 hour DW10B engine test following the CEC method [10] using valve covered orifice injectors and the same CEC-specified test fuel containing 1 mg/kg Zn, as used in the CD test.

Table 1: Abbreviations used to describe the different tests, with power loss data taken from reference [15, 16].

Abbreviated Injector name	***Test***	***Power loss (%)***
CD DU	Chassis Dynamometer Dirty-Up test	-5%
DW10B DU	CEC DW10B Dirty-Up test	-7%

During both tests, engine power loss was measured as an indicator of deposit build up in the nozzles. The results (reported in reference [15]) demonstrated substantial power loss in both cases over the course of the test cycle (≥5%).

After testing, the injectors were removed from the engines for the analysis reported in this manuscript.

Sectioning

A new sectioning approach has been developed to reveal entire channels of injector nozzles without the use of chemicals (Figure 1). Chemical free sectioning is attractive for high resolution chemical analysis of carbonaceous deposits on metal substrates.

First, the location of the channels was clearly marked near the exit of the nozzle. Second, two cutting stages were involved to reveal the interior of the channels. The first cut was made, using a mini silicon carbide saw, perpendicular to the axial direction of the injector, approximately 8mm from the injector head (Fig 1b). As the injector and nozzle hole diameter (0.1mm) are relatively small, a 10x optical microscope lamp had to be used to increase the visibility and cutting accuracy. The second cut was made along the marked channel lines to reveal the channel section along the axial direction. Due to the small diameter of the channel (0.1mm), to avoid over cutting the channel, this cut was made ~0.2mm in front of the channel (Fig 1d). The channel was carefully revealed by grinding using SiC media (Fig 1e). During this grinding step, progress was monitored using an optical microscope to ensure that the channel was revealed with an even polish. Because of the angles involved, it was usually only possible to fully expose one channel. Additionally, the exposed channel had to be as shallow as possible to avoid problems with further TEM sample preparation. Swarf generated during this sectioning process was removed using a magnet and a final clean was performed using a jet of compressed air.

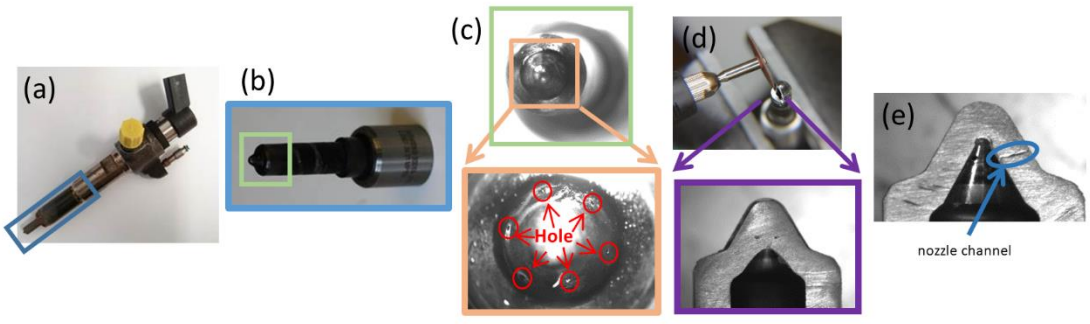

Figure 1: Sectioning of Injectors (a) a 'CD DU' *injector. (b) The enlarged view of the injector head as highlighted in the blue box in (a). (c) a close top view of the injector head and the inset shows the enlarged view of the top view of injector head for which the locations of nozzle holes are marked in red circles. (d) The second cut on the injector head along the axis direction using a mini silicon carbide*

cutting wheel, an enlarged side view is shown in the inset. (e) The section view of the finial finishing of the nozzle head. The exposed channel is marked using the blue ellipse.

Focussed Ion Beam SEM (FIB-SEM) lift out

Cross-section samples for high resolution TEM analysis were removed from the nozzles using the FIB lift out technique [17]. This works by combining an SEM for imaging with a gallium ion beam which is used to cut into the sample (Fig 2a). The electron and ion beams are positioned such that when the sample is tilted to 52˚ it is perpendicular to the ion beam, and when it is at 0˚ it is perpendicular to the electron beam. This means that the sample can be milled and imaged simultaneously at both angles depending on the milling that is required. Typical samples prepared using FIB lift out are relatively flat, but in our case we had a region of interest that firstly had high roughness and secondly was deep within the cross sectioned nozzle, which (depending on how it is sectioned) could be up to ~100 µm deep (the diameter of the nozzle hole). This causes logistical problems as the full region of interest must be visible at both 0˚ and 52˚ without being obscured by the sides of the trench. Additionally, the omniprobe micromanipulator, which is used to remove the region of interest after milling, cannot come into contact with the sides of the nozzle as it tries to remove the sample. This presents a challenge with narrow and deep trenches and motivated the development of a precise macroscopic sectioning process.

Here we summarise the FIB-SEM lift-out technique employed for our sample preparation within the FEI Helios NanoLab 600. A suitably shallow region of the nozzle is located that does obscure the image at the tilt angles used and will not cause problems for the omniprobe in lifting out the sample. A protective layer of platinum is deposited so that the region of interest (ROI) is not damaged by the gallium ion beam (~17 x 2.5 µm area, and 4-8 µm depth). The sample is tilted to 52˚ and on three sides of the ROI trenches are milled using the ion beam to a depth of about 10 µm (Fig 2 c and d). The sample is then tilted to 7˚ and the ROI is undercut so that it is only attached by one small region. The omniprobe micromanipulator is attached to one corner using local ion beam deposition of a platinum rich layer (Fig 2 c and d) and the remaining section (which can be seen on the right of Fig 2d) is cut, enabling removal of the sample using the omniprobe. The sample is then moved to an omnigrid which is the correct size for putting in the TEM, and attached using a platinum rich deposition (Fig 2e). The omniprobe is then detached from the sample using the ion beam and the cross section is then milled using decreasing beam currents, until it is electron transparent (~70 nm) (Fig 2f).

The SEM was operated at 5kV and 0.17 nA. For coarse milling the ion beam was operated at 30 kV and a beam current of 0.92 nA. The voltage and beam currents were reduced in stages for the final thinning and polishing steps to make the sample electron transparent.

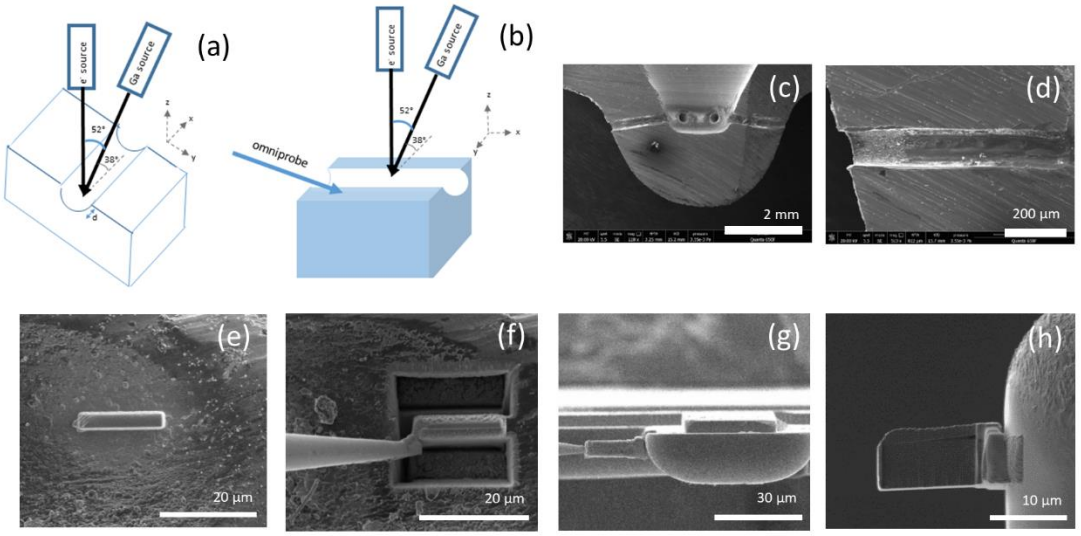

Figure 2: FIB liftout (a) and (b) Schematic of sample orientation relative to the incoming electron and ion beams from two perspectives. These highlight the difficulty in removing a region of interest from a non-flat surface ; (c) Cross sectioned injector tip and (d) higher magnification of the cross sectioned nozzle channel showing the roughness and therefore difficulty in extracting an ROI from the channel; (e) a protective layer of Pt is deposited over the region of interest; (f) SEM image showing the trenches that have been milled around the Pt and an omniprobe micromanipulator is attached to the sample prior to it being cut free from the bulk; (g) The cross section is moved using the omniprobe, to the TEM grid and attached using Pt. It is then cut free using the ion beam. (h) Finally the sample is thinned to electron transparency (<100nm) using the ion beam.

Scanning Electron Microscopy (SEM) and Energy Dispersive X-ray Spectroscopy (EDS)

After sectioning, the injectors were first investigated using Scanning Electron Microscopy (SEM). Typically SEM is used to study structures from a few millimetres down to ~50-100 nm in size. For imaging the cross sectioned injectors, we employed secondary electron imaging where secondary electrons (SE) are generated by the incident fast electron from a few nanometres below the surface. SE imaging therefore helps us visualise the surface structure and morphology of the injectors covering a range of different lateral length scales.

Combined with this, site-specific chemical information can be collected simultaneously using energy dispersive X-ray spectroscopy (EDS). The incoming fast electrons can promote electrons within the sample to higher energy states. These electrons subsequently fall back down to their lower energy configuration, releasing characteristic X-rays. Measured X-rays are generated from deeper within the sample than SEs. This means the chemistry being probed is an average of the chemistry through the volume of region in which the primary electron beam interacts (beyond the location where the secondary electrons are generated). As the energy of the incident electron increases (i.e. as the operating voltage of the microscope increases), the X-rays generated come from deeper within the sample and from a wider lateral distance (due to greater scattering within the sample). This results in poorer spatial resolution than the equivalent SE image. The precise spatial resolution of EDS depends on factors such as probe size and voltage, as well as the chemistry and structure of the target sample. In the SEM, EDS typically has a resolution ranging from tens of nanometres to one micron. In the TEM, the resolution of EDS is increased because the sample is thin and therefore an EDS signal is only generated from a volume equivalent to the incoming probe diameter and the thickness of the thin foil sample.

One further complication arises from the generation of lower energy X-rays deep within the sample, as they may not escape the sample and this can further limit quantitative assessment.

Since a higher operating voltage results in the X-ray signal being generated from a greater depth below the surface, thin layers of deposit (a few 100 nm) may not be observed with the higher voltage incident electron beam as the underlying steel of the injector will dominate the signal. Similarly, lower operating voltages will only probe the surface chemistry and will ignore the composition of thicker deposit. For the samples presented in this work operating voltages of 10 and 20kV were used in the SEM as a compromise between investigating the relatively thick deposit, and capturing the signal from all elements present.

SE imaging was carried out on an FEI Quanta 650F Field Emission Gun SEM (FEG-SEM) using an SE detector and operated at 10kV and 20kV. The spot size was optimised to obtain the best signal for chemical mapping. EDS analysis was carried out using a 60 mm^2 (<126 eV energy resolution) Bruker XFlash®6 spectrometer with Quantax 800 (BrukerNano GmbH, Berlin, Germany). These operating voltages were used to ensure X-ray signals from all the elements of interest were collected with high efficiency. Maps were acquired from the regions of interest with constant scanning of the electron beam. Each map was acquired for about 10 mins.

EDS data was processed using the Bruker Esprit2 software and for SEM based studies, qualitative assessment of the data was carried out. While it is possible to undertake quantitative EDS analysis,

the roughness and variable density of our carbonaceous films makes this challenging. In particular, the depth of the nozzle channel can affect the line of sight between the generation of X-rays in the sample and the EDS detector. Data from these maps must be interpreted with care by taking these effects into consideration. We cannot with confidence report fully quantified results from EDS analysis of these regions and we caution against direct comparison of absolute values with other reports of similar deposits [9, 18]. Our concern about quantification of these results motivated our TEM studies, which are reported in the next section.

Scanning Transmission Electron Microscopy (STEM)

To investigate cross sections of the deposit down to the nanoscale, scanning transmission electron microscopy (STEM) was used. STEM operation is similar to that of SEM using a rastered beam of electrons, but instead the sample is a thin foil and the transmitted signal is collected on an annular detector located below the specimen. The collected signal is proportional to the atomic number squared and the density of the material. Hence, regions of higher atomic number or thickness will appear brighter in STEM images.

While the STEM probe is being rastered across a region of interest an EDS chemical map can be obtained concurrently, as for SEM. The depth resolution of the resulting map is of the order of a few tens of nanometres (i.e. the foil thickness of ~70-100nm), compared with hundreds of nm for the SEM. This is a significant attraction of TEM based EDS analysis. TEM-EDS also has much higher spatial resolution (~10 nm) which means a nanoscale chemical map can be obtained. If the sample is flat and of consistent density then the chemistry can be fully quantified. For this work, we utilise STEM based EDS analysis to probe for the localisation of deposit chemistry and to quantify the relative chemistries in the selected region. Because of the nanoscales involved, this does not give a quantitative view of the total deposit in the sample.

STEM work was carried out on an FEI Titan 80-300 S/TEM microscope equipped with a Schottky FEG and operated at 80kV and 300kV with a beam convergence angle of 14mrad. The acceptance angle to the high annular dark field (HAADF) detector is 40-196 mrad. There was no noticeable damage to the sample at either operating voltage at the magnifications at which the sample was investigated.

EDS maps were acquired on a Bruker XFlash®6 spectrometer with windowless detector. Data was processed using the Bruker Esprit 2 software using the Cliff-Lorimer quantification method. This used calculated k-factors and the background regions and elements present were selected manually. Elements such as Pt and Ga from the FIB milling and Cu from the omnigrid were included for the

quantification procedure, but the compositions reported have had these elements removed to better reflect the composition of the deposit.

(3) Results + Discussion

SEM - Structure, Morphology and Chemical Analysis

From the SEM cross sections it was clear that, whilst deposit was present along the full length of the nozzle channel, the deposit was thicker at the nozzle hole outlet for both the CD DU and DW10B DU samples. Deposit morphologies in the DW10B CD sample and the CD DU sample are similar, however the DW10B CD deposit appears to be much thicker and contains larger diameter features.

EDS maps were taken of the deposits in the region of the nozzle hole outlet containing the thickest deposit in each sample, (Fig. 3). The maps shown in Fig 3 are for the most abundant elements present in each sample – C, O Zn and Fe. Both samples also contained trace elements such as Ca, S and Si; (See Fig 5a and 6a for TEM EDS spectra from a region of the deposit). For both samples the deposit was composed primarily of C, O, and Zn sitting on a predominantly Fe (steel) substrate. There was a much stronger C signal from the CD DU than from the DW10B DU – the first indication that the composition of the deposits is in fact different. (The contrast for the C signal has been enhanced for the DW10B DU to highlight the morphology rather than composition).

For the CD DU sample, the deposit morphology is predominantly bulbous in nature except towards the nozzle outlet where the deposit is smoother and flatter. This smooth, flat morphology at the outlet has been observed previously where deposition has not been uniform around the outlet [18]. The EDS maps suggest that C and O have co-deposited and have a relatively smooth morphology, with Zn visible in the cracked regions of the deposit. At first glance this may look as if Zn has deposited in the cracks. However, it is more likely that a continuous layer of Zn has deposited first, on top of which C/O has deposited. The C/O deposit has then cracked revealing the Zn layer underneath. Due to the thickness of the deposit in this region the EDS signal will only probe the top surface, hence the top deposit, which is C/O based, is clearly visible, but the underlying deposit (Zn based) is not. This is why Zn is observed in the regions where the C/O deposit has cracked. To probe the full depth of the layered deposit structure the sample must be cross sectioned and studied using TEM. C and O are co-localised but Zn and O do not appear to be. It also looks as if there is no Zn at the very edge of the nozzle outlet, however, this again is most likely due to the EDS signal being obscured by the thick C/O deposit on top

of it. We have reported previously that in the case of CD DU the cracks act as secondary nucleation sites for deposition and growth [5].

In the DW10B DU sample, the deposition appears to have occurred by a different mechanism. The C and O appear to have similar bulbous morphology suggesting that the C and O have co-deposited in the same regions. The O signal was stronger suggesting that O is more abundant than C. In the O map, however, cracks in the deposit are visible which, although present in the C map, are not as obvious. The cracks match those observed in the Zn map well, suggesting that O may have co-deposited with the Zn as well as the C. This would also explain the higher abundance of O relative to C. The morphology of the Zn map is significantly different from that of the C and O - it is much smoother. This suggests that although O is present in both the C and Zn deposits, there are different deposition mechanisms resulting in these different morphologies. Close inspection of the O map reveals that it has some C-like and some Zn-like character, confirming this hypothesis.

There are multiple deposition mechanisms occurring in sample, as there is significant variation in the chemistry and morphology of the deposits, despite the same elemental species being present in each.

Whilst SEM and SEM-EDS give an excellent overview of what is happening in the sample, there are a number of questions that cannot be resolved using this technique. SEM imaging is able to tell us what is happening at the surface of the sample, but very little about the underlying structure and chemistry. It also has limited spatial resolution for both imaging and chemical mapping. For our samples, the roughness of the sample also makes interpretation, particularly of chemical information, difficult, and full quantitative analysis is not possible.

To fully understand the chemistry and structure of the deposits below the surface, a cross section of a region of interest needs to be prepared. A cross section can be obtained using FIB-SEM to highlight a region of interest and milling out a lamella which can then be thinned to electron transparency (~70-100 nm). This is then put into a TEM to obtain structural and chemical information about what is happening under the surface. A full analysis of the FIB-SEM preparation is described in the experimental section.

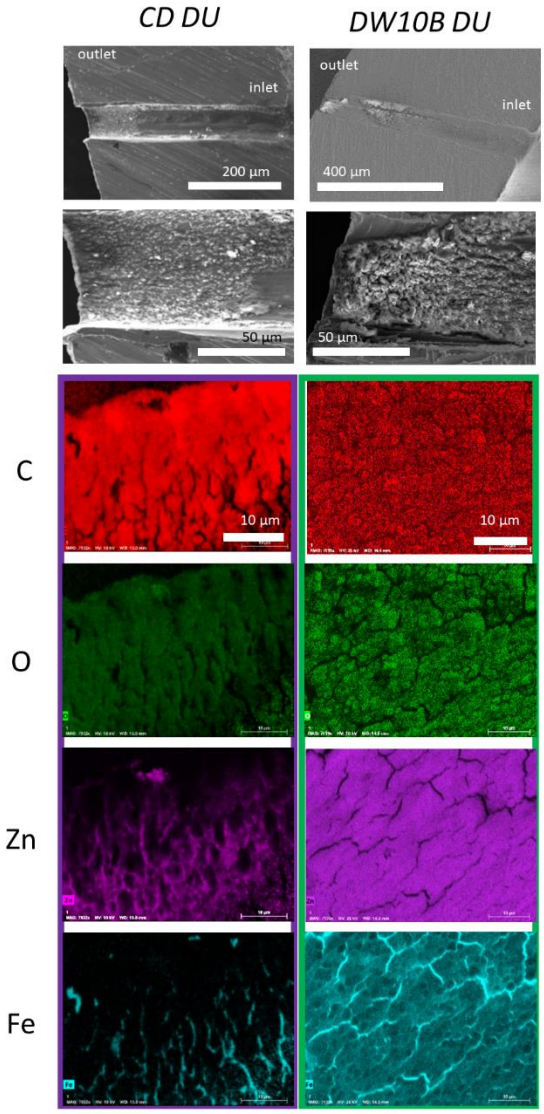

Figure 3: SEM images of nozzle and outlet region (previously shown in SAE), and EDS maps of the dominant elements (C, O, Zn and Fe) at the nozzle outlet

STEM Structure and Morphology

The electron transparent cross sectional samples were imaged using Scanning Transmission Electron Microscopy (STEM). In this mode heavier elements appear brighter and so the protective Pt layer deposited in the FIB, and the steel substrates, appear particularly bright in the lower magnification images (Fig. 4c). Because the samples are so porous, nano-sized bright dots also appear within the deposit layer – these are Pt particles from the surface protective coating that have deposited deeper within the sample through the porous structure.

For our samples, an advantage of the protective platinum-rich layer is that it highlights the roughness of the deposited layers (Fig 4a,c). The DW10B DU has much higher roughness (~1-4 µm with a total depth of deposit up to ~6 µm) than the CD DU sample (~1 µm and a total deposit thickness of ~ 1-2 µm). The thickness estimates are based on the cross sections being taken from the sample near the nozzle outlet, which had the thickest region of deposit and these values broadly agree with the SEM results. The exact thickness of the deposit varies due to the inhomogeneity of the deposit along the length of the injector nozzle hole. Both samples were taken slightly away from the nozzle hole outlet and it is possible that the deposits at the outlet were slightly thicker than those sampled in both the DW10B DU and CD DU nozzles.

In both samples, there is significant porosity through the thickness of the deposit, which is not observed from the top-view SEM images. The CD DU sample has large variation in pore size in the 'small pore' regime (<1 µm). In addition to pores in this size range, the DW10B DU sample also has larger, micron sized pores which were not observed in the CD DU sample. Additionally, the greater roughness in DW10B DU means that there are also larger gaps between different bulbous features in the layer.

There is a layered structure parallel to the steel substrate that appears in each of the samples showing that the deposition is not uniform across its thickness even within one sample. Whilst both samples exhibit this banding, it is on a different length scale within each sample.

In the CD DU sample there are two distinct layers which appear as bands in the cross section (Fig 4a-b): one dense and wide ~80-105 nm band; and one narrower ~40-80 nm and more porous band. The thickness of the band pairs increases together (i.e. the widest part of the wide band was located next to the widest part of the narrow band). The number of bands also varied across the specimen with some regions having 16 bands (counting dense and porous as two separate bands) and others having 5 bands. These banded layers were formed on top of regions where clear bands were not observed, and towards the top surface of the deposit the banding morphology was similarly unclear.

In contrast, whilst the DW10B DU sample also contains banding, it has a different morphology and is only clear in regions of the cross section that were not thinned sufficiently in the FIB-SEM. In the thinner regions of the cross section it is difficult to distinguish the banding structure (Fig 4c-d). The morphology is different to that of the CD DU sample as each DW10B DU layer has a porous structure. The banding pattern comes from joins between adjacent layers of porous material rather than alternating porous/dense layers. Each band is about 80-90 nm in depth and there are approximately 12 bands in the thickest regions of the deposit.

In both cases the banding appears to be due to a periodic event in the deposit formation test. In the CD DU test there are two possible events which could explain the banding. Firstly, a Diesel Particulate Filter (DPF) regeneration occurred three times in the test. During this event, the injection strategy is altered to include injection of fuel late in the engine cycle leading to increased hydrocarbons at the injector nozzle and there is a potential impact on deposits. However, there are more than six bands (three times of regeneration) in the CD DU deposit strata and so the alternation between normal running and DPF regenerations are unlikely to explain the banding. Secondly the CD DU test uses a cycle containing periods of normal steady speed driving load and higher loads with roughly equal periods of each in the 30 minute cycle time [14]. These differences in load intensity (thus temperature) could lead to different deposit formation conditions which are evident in the deposit strata, but there are more cycles in the test (48, therefore 96 alternations) than bands in the deposit. This could be explained by a deposit induction period occurring during the initial cycles during which deposit precursors from combustion are consumed in the formation of a deposit initiation layer, which once formed constitutes a foundation layer for carbonaceous deposits to build upon in latter engine cycles. Despite the large discrepancy between number of load alternations and number of layers, this appears to be the most likely explanation for layering in the deposit in this sample.

The DW10B DU test uses a 1 hour cycle comprising 12 stages which alternate between low and high load operation. Given the short residency of the engine at each load point it is unlikely that this load switching could be detected in the deposit strata of samples from this test. Unlike the CD DU test, the DW10B test [10] has an engine-off period of 4 hours after every 8 cycles of running, (with 32 cycles in total/three intermediate engine off periods). During this period the engine cools down and subsequently heats up again during the following running period. In the DW10B DU test, these thermal cycling events are thought to be the most likely cause of the deposit banding as there are similar numbers of bands and thermal cycling events.

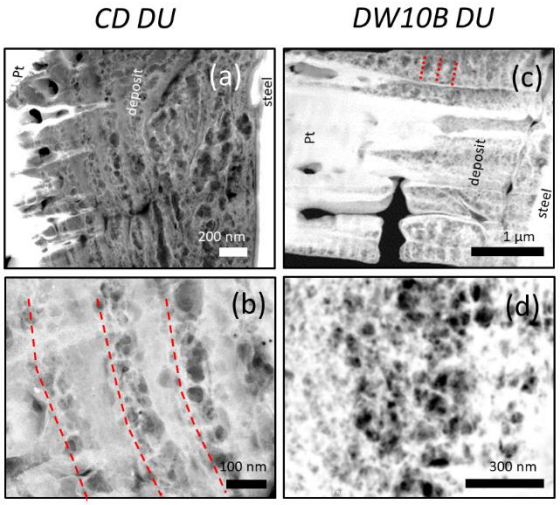

Figure 4: STEM of deposit cross section for CD DU test and DW10 test. (a) low magnification image of CD DU sample showing porous and banded structure of the deposit. The bright regions are the steel and Pt deposited layer which appear bright due to their higher atomic number. (b) higher magnification image showing bands of denser material interspersed with more porous layers (c) Low magnification image of DW10B DU sample showing the thickness, roughness and large scale porosity of the deposition layer. (d) higher magnification region showing the porosity of the structure. The dotted red lines in b and c highlight some of the banding structure.

STEM Chemical mapping of bulk deposit

Chemical analysis of the deposit cross sections was performed using STEM-EDS. EDS results of the CD DU cross section are found in Figure 5. The banded structure observed in the STEM images clearly translates to the chemical signal seen in the EDS maps (Fig 5b). As observed in the SEM-EDX, C, Zn and O are the most abundant elements in the deposit and are present right down to the steel interface. There is a higher concentration of Zn and O closest to the steel substrate with very little C present. This confirms the earlier suggestion that Zn and O co-deposit, and deposit fairly uniformly in the initial few hundred nanometres of deposit-material. It is only in the subsequent layers that significant carbon deposits appear. Within the banding region (>0.5 µm from the steel surface) we see more C deposit and the C and Zn deposits grow in alternate layers - the Zn signal peaks where the C signal dips and vice versa – showing that there is a sequential deposition of Zn and C elements. The oxygen signal is fairly uniform throughout the sample, though there is some indication that there is a slight increase with the carbon signal in the bulk of the deposit in the upper layers. By overlaying the

chemical maps with the STEM images it seems that the denser layers are C/O based, and the more porous layer is Zn/O-based.

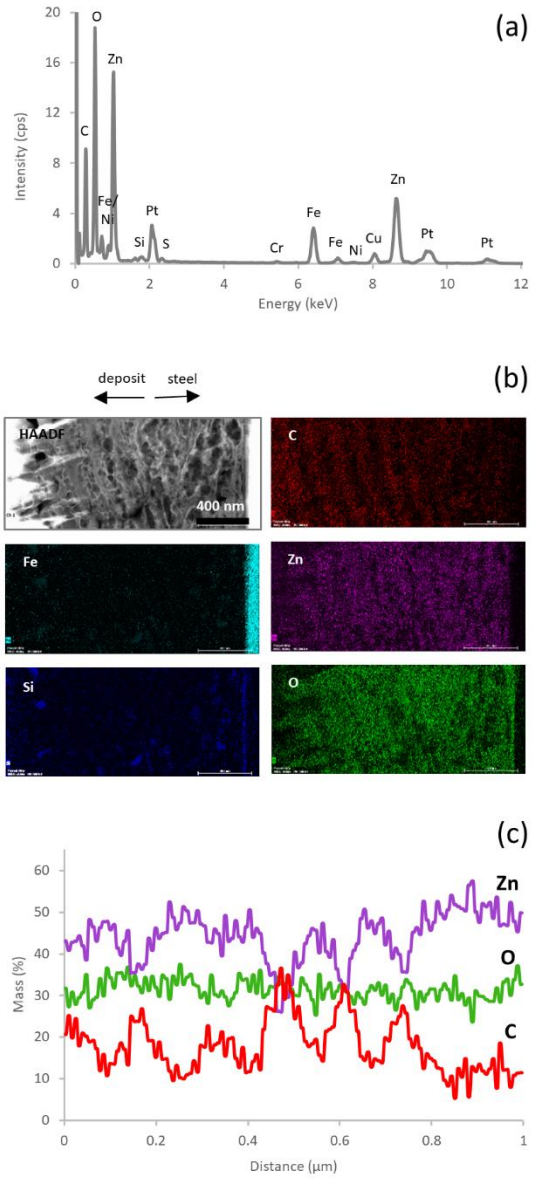

Figure 5: Chemical map of cross section of deposit in CD DU test sample. (a) EDS spectrum from the whole region analysed; (b) SE image and EDS maps of the most abundant elements – Zn, C and O; (c) a line profile of the elemental distribution of Zn, C and O across the bulk deposition layers. The contrast in the maps has been enhanced where necessary to show the deposit clearly. This is not indicative of the actual percentage of each element present in the sample.

The chemistry of the DW10 DU cross section (Fig 6) is different to the CD DU sample. Here the deposit is predominantly Zn and O with a minimal C signal. Additionally, there are a large number of trace elements (Fig 6a) which are evenly distributed throughout the whole of the deposit layer. In this sample the carbon signal was very low, a similar level to that of the trace elements. The maps in Fig 6b indicate that C concentration is higher in some of the regions that have lower Zn concentration. However, this also coincides with the bright regions in the HAADF image and so is more likely due to deposition of platinum (which is associated with carbon due to its production in the electron microscope) reaching into the porous structure. The banding structure observed in the TEM images is not reflected well in the chemical maps indicating that the banding is not predominantly due to a change in chemical composition and must therefore be related to changes in structure and density.

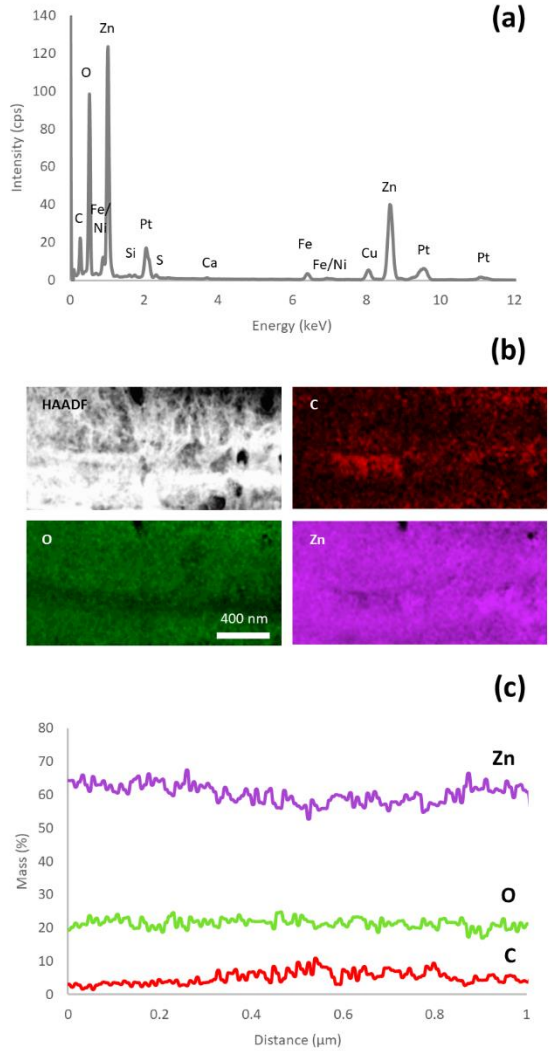

Figure 6: Chemical map of cross section of deposit in DW10B DU sample. (a) EDS spectrum from the whole region analysed; (b) STEM image and EDS maps of the most abundant elements – Zn, C and O;

(c) a line profile of the elemental distribution of Zn, C and O across the bulk deposition layers. The contrast in these maps has been altered to allow the deposits to be more clearly visualised.

A direct comparison of the elemental composition of both samples is shown in Figure 7. This clearly shows that the CD DU sample has more carbon/oxygen material and the DW10B DU sample is richer in zinc/oxygen.

(a)

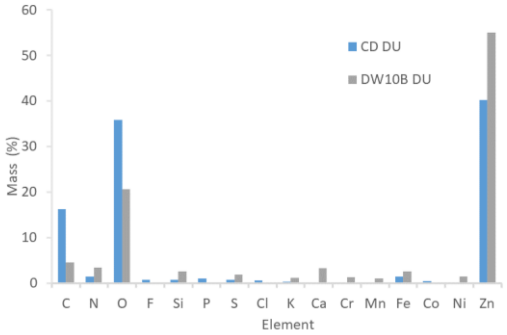

(b)

	C	N	O	F	Si	P	S	Cl	K	Ca	Cr	Mn	Fe	Co	Ni	Zn
CD DU (mass %)	16.3	1.4	35.9	0.7	0.7	1.0	0.8	0.6	0.4				1.4	0.5		40.3
CD DW10B (mass %)	4.5	3.4	20.6		2.5		1.9		1.2	3.2	1.3	1.0	2.5		1.5	55.0

Figure 7: Comparison of chemical composition of the deposit from CD DU and DW10B DU injectors.

STEM Chemical mapping of interface

The CD DU sample contained a variety of trace elements (Fig 5a). A Si-rich layer (20 nm) is concentrated below the zinc oxide layer and on top of an iron oxide layer (10 nm) on the steel substrate (Fig 5b).As this layer was only found in one of the samples and both samples were generated using the same fuel, it is thought unlikely that the Si originates from the fuel. The origins of Si are unclear, but may have been introduced during fabrication of the nozzles themselves as inspection of a new nozzle suggested. Between the steel and the iron oxide layer there is a Ni rich layer (~2 nm), which has a Cr rich layer on top of this (~5 nm). It is likely that these layers are generated either during

the manufacturing process or through Cr and Ni segregation of the steel due to the high temperatures experienced in the nozzle (Fig 8a).

For the DW10B DU the layers formed at the interface are much wider than they are in the CD DU deposit. The main interfacial deposits in the DW10B DU sample are Cr, P, K and Mg (Fig 8b – only Cr, P and K are displayed for the sake of clarity) with at least two layers of P present. The K and P layers are about 100 nm in depth. Where the P and K are present, Zn and O are also present (not shown), so the P and K co-deposit with the majority elemental deposits. The Cr layer is not unexpected and can be explained as Cr segregation to grain boundaries and the surface of the steel during heat treatment. The K and P may be intrinsic to the steel itself, may have been deposited during the manufacturing process, or a layer may have formed on the surface of the steel from elements present in the fuel and lubricant.

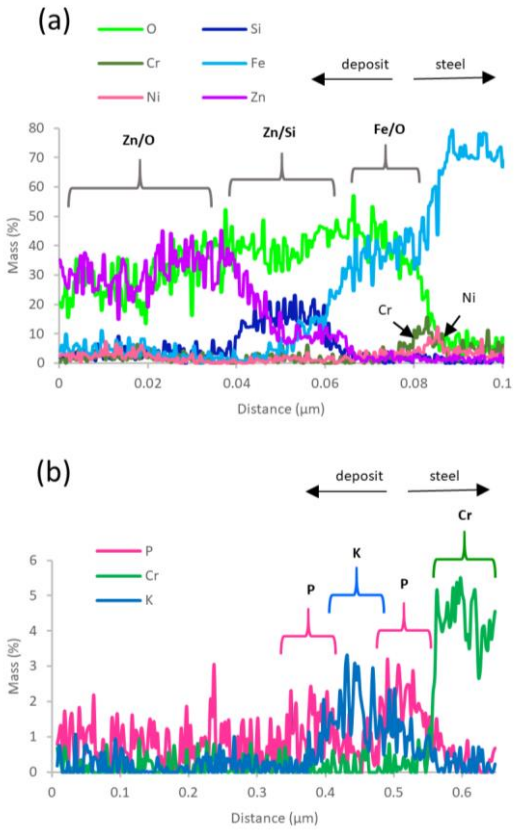

Figure 8: Chemical map of interface of steel and deposit in (a) CD DU and (b) DW10B DU samples. (a) The main elements present across the interface for CD DU; (b) The 'significant' minor elements present at the steel/deposit interface for DW10B DU

Based on these results, Figure 9 shows a schematic of the main elements present at the interface of each of the samples. The exact widths of layers and the abundance of the minor elements varies between regions.

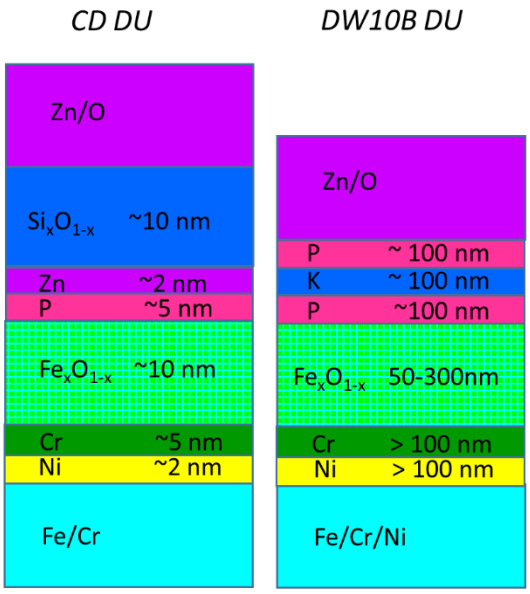

Figure 9: Schematic of the interface structure for the CD DU and DW10B DU samples. In the DW10B sample there was a lot of variation in the FeO layer width and the composition of minor elements at the interface.

The results from TEM analysis largely agree with what was observed in SEM [5] but provide a richer understanding of the microstructure and chemical composition of the deposit down near the interface itself. Without this high resolution of the cross-sectional information it is impossible to deduce the structure/chemical composition of the deposit as it has deposited/grown from the steel interface upwards. It is also not possible to make any quantitative measurements in terms of deposit depth, spacing between deposition regions or quantitation of chemical species. For example for the CD DU sample SEM suggested that in the bulk of the deposit there were regions with C and O co-located, and uniform Zn throughout. However, when we compare this with the TEM analysis we see that there is a very clear alternating C/Zn structure whereas oxygen is located uniformly across the sample. In the thin deposit region we saw from SEM that the deposit was predominantly Zn and O with only a little C – TEM largely agrees with this (noting that the SEM does not identify thin layer structures of Si, Ni and Cr near the metal substrate).

Similarly, for DW10B DU from the STEM-EDS, it looks like C, O and Zn were all deposited in similar locations, but on inspection of the TEM data it is clear that the deposit is mainly Zn and O with minimal C. Additionally, although some banding is present in the deposit structural morphology, this is not evident in the chemical map, showing that the deposition mechanism is quite different to that of CD DU, with C, O and Zn co-depositing. This cannot be observed from SEM analysis alone. Similarly, SEM does not show the concentration of trace elements at the interface between the deposit and the steel.

When comparing the findings from this work to those from previous studies applying commonly used analytical methods such as SEM [11,12] it is apparent that deposit formation in diesel injector nozzles can share some similarities such as in the primary constituents of the deposit – C, O and Zn, when a Zn fouling agent is used in the fuel. However there are distinct differences apparent from the deposit morphology that indicate that different mechanisms are in play depending on the engine type, duty cycle and inevitably the fuel composition. Within the current study, where the same fuel composition has been used in similar light-duty (LD) engine technology, albeit with different injector designs (VCO and mini-sac nozzles) and test cycles moderately different in severity, the novel application of FIB and STEM have enabled distinct differences in deposit morphology and local composition on the nanoscale to be identified which has confirmed that different deposit mechanisms are in play. This work gives new insight into the growth of deposits through the cross section of the deposit enabled by the application of FIB and STEM techniques. The banded layer structure of deposits is present after CD DU testing but not after the DW10B DU test. From this initial work, it is unclear what controls the thickness and layering within the CU DU structure and ideally further testing would correlate loading cycles (with periodic injector extractions) with the formed layers to extract what controls the structural and chemical variation in this sample. The relative absence of the layered structure in the DW10B DU test indicates that the mechanisms of deposit growth varies between the CD DU and DW10B DU tests.

(4) Conclusions

We demonstrate for the first time in this field, that the hierarchical structure and chemistry of deposits can be probed from the micron to nanoscale using electron microscopy techniques. This is only possible by careful sample preparation which preserves the original structures being studied – mechanical sectioning to reveal the channels and FIB-SEM sectioning to provide electron transparent samples for transmission electron microscopy studies. Using these techniques the underlying deposit structure has been studied for the first time.

Whilst SEM has provided great insight into the deposition mechanism and surface chemical analysis, real understanding of the mechanisms by which deposit formation occurs can only start to be addressed once information about the initial deposition layers is obtained. Despite the two samples studied here appearing to have similar morphology and chemistry in the SEM data, the structure and chemical make-up is found to be quite different through the sample's cross section. Cross sections of the deposit reveal the sub-surface, porous morphology of the deposit layers. Both samples contained sub-micron-sized pores but the DW10B DU deposit was much rougher and contained larger, micron sized pores. A banding structure was observed in both sample morphologies but only in the CD DU sample was this clearly related to the chemistry – alternating C and Zn layers. The deposit composition was found to be different across the two samples – the CD DU contained both Zn and C as the dominant elements whilst DW10B DU was predominantly Zn based. Chemical mapping also revealed the presence of thin (<10 nm) layers of deposit at the interface with the steel, though further work would need to be carried out to determine where these have come from and how they affect the subsequent deposition. Combining this knowledge could lead to identifying more accurately the chemicals and processes involved in deposition and modifying the contributory processes to achieve reduced deposition in the future.

Whilst the macro scale deposit is what impedes the flow of fuel in the nozzles, an understanding of the nanoscale interactions, as the deposit initially forms on the steel, is essential to fully comprehend the deposition mechanism. Without understanding the nanoscale, deposition can never be fully eradicated. Our results show that by using TEM techniques to probe the nanoscale, interface deposition layers have been identified which would otherwise not have been observed. The impact these have on deposit formation and growth has yet to be determined, but the results highlight that without TEM, a very important piece of information is missing which may influence changes in test cycles or fuels in the future.

The findings here have importance for methods designed to model real world deposit formation under controlled conditions. They show that relatively small differences in injector design and/or test cycle severity can have a substantial impact on deposit formation mechanisms leading to different composition and morphology characteristics. Furthermore, a range of deposit mechanisms have been identified across a range of test scenarios. Therefore this work shows that it is important to consider a range of test scenarios to develop deposit understanding which is representative of all real world scenarios. The influence of engine operation in deposit formation demonstrated through the identification of repeated strata in the deposit is a key finding and leads the way for further studies which purposely isolate and characterise the specific impact of different engine operating conditions on deposit formation.

Acknowledgements

This work was funded through two Shell University Technology Centres hosted at Imperial (Fluids & Lubricants, and the Advanced Interfaces in Materials Sciences). TBB acknowledges funding from the Royal Academy of Engineering for his Research Fellowship.

Author Contributions

JJ performed mechanical sectioning of the injectors. CMM conducted the electron microscopy & FIB sample preparation. The initial project was designed and planned by FG, TBB, RW and NR. CMM drafted the first manuscript. All authors have helped edit and refine the final manuscript.

References:

1. Leedham, R. Caprotti, O. Graupner, and T. Klaua, "Impact of fuel additives on diesel injector deposits," *SAE Technical Papers,* 2004, doi: 10.4271/2004-01-2935.
2. R. Caprotti, N. Bhatti, and G. Balfour, "Deposit control in modern diesel fuel injection systems," *SAE International Journal of Fuels and Lubricants,* vol. 3, pp. 901-915, 2010, doi: 10.4271/2010-01-2250.
3. Montanaro and L. Allocca, "Impact of the nozzle coking on spray formation for diesel injectors," *SAE Technical Papers,* vol. 11, 2013, doi: 10.4271/2013-01-2546.
4. Hoang, AT. and Le, AT., "A review on deposit formation in the injector of diesel engines running on biodiesel"," *Energy Sources, Part A: Recovery, Utilization, and Environmental Effects,* 41(5) pp 584-599, 2019, doi: 10.10.1080/15567036.2018.1520342
5. Caprotti, R., Breakspear, A. and Graupner, O., "Beyond 2008: The challenges for diesel detergency'', TAE Esslingen Symposium 2007.
6. Bennett, J. and Lau, T.L., "Diesel Fuel Additives as a Route to Vehicle Fuel Efficiency Improvements", 17th Annual Fuel & Lubes Asia Conference, 2011.
7. Barbour, R.; Arters, D.; Dietz, J.; Macduff, M.; Panesar, A.; Quigley, R.: Injector Fouling Effects in Modern Direct Injection Diesels. 13th Fuels & Lubes Asia Conference, 2007.
8. Hawthorne, M., Roos, J., Openshaw, M. "Use of Fuel Additives to Maintain Modern Diesel Engine Performance with Severe Test Conditions", SAE 2008-01-1806, doi:10.4271/2008-01-1806
9. Birgel, A, Ladommatos, N., Aleiferis, P., Zülch, S., Milovanovic, N., Lafon, V., Orlovic A., Lacey P., and Richards, P., "Deposit Formation in the Holes of Diesel Injector Nozzles: A Critical Review", SAE 2008-01-2383. SAE 2008-01-2383, doi:10.4271/2008-01-2383
10. Co-ordinating European Council CEC SG F-098; "Direct Injection Common Rail Diesel Engine Nozzle Coking Test", http://www.cectests.org/
11. Tang, J., Pischinger, S., Lamping, M., Körfer, T., Tatur, M., and Tomazic, D., "Coking Phenomena in Nozzle Orifices of DI-Diesel Engines'', SAE 2009-01-0837, doi: 10.4271/2009-01-0837

12. Ikemoto, M., Omae, K., Nakai, K., Ueda, R., Kakehashi, N., and Sunami, K. “Injection Nozzle Coking Mechanism in Common-rail Diesel Engine”, JSAE 2011-9067 / SAE 2011-01-1818, doi:10.4271/2011-01-1818
13. Barker, J., Reid, J., Angel Smith, S., Snape, C., Scurr, D., Langley, G., Patel, K., Carter, A., Lapthorn, C. and Pullen, F., “The Application of New Approaches to the Analysis of Deposits from the Jet Fuel Thermal Oxidation Tester (JFTOT)”, SAE Int. J. Fuels Lubr. 10(3):741-755, 2017, doi:10.4271/2017-01-2293
14. Williams, R., Smith, A., and Buttery, I., "Formation and Removal of Injector Nozzle Deposits in Modern Diesel Cars," *SAE Int. J. Fuels Lubr*. 6(1):230-240, 2013, doi:10.4271/2013-01-1684.
15. Rounthwaite, N; Williams, R; McGilvery, CM; Jiang, J, Giuliani, F. and Britton, T.B. A Chemical and Morphological Study of Diesel Injector Nozzle Deposits – Insights into their Formation and Growth Mechanisms. *SAE Int. J. Fuels Lubr.* 2017;1:10
16. Smith, A and Williams, R. Linking the Physical Manifestation and Performance Effects of Injector Nozzle Deposits in Modern Diesel Engines. *SAE Int. J. Fuels Lubr.* 2015;8:344-357
17. Langford, R.M. and Clinton, C. “In situ lift-out using a FIB-SEM system, *Micron 35 (2004) 6007-611*
18. Risberg, P.A. and Alfredsson S. “The Effect of zinc and other metal carboxylates on nozzle fouling” *SAE Technical Paper 2016-01-0837;*